New Chondritic Bodies Identified in Eight Oxygen-bearing White Dwarfs

Alexandra E. Doyle[1] , Beth L. Klein[2] , Patrick Dufour[3,4] , Carl Melis[5] , B. Zuckerman[2] , Siyi Xu[6] ,
Alycia J. Weinberger[7] , Isabella L. Trierweiler[1,2] , Nathaniel N. Monson[1], Michael A. Jura[2,8], and Edward D. Young[1]
[1] Earth, Planetary, and Space Sciences, University of California, Los Angeles, CA 90095, USA; a.doyle@epss.ucla.edu, eyoung@epss.ucla.edu
[2] Department of Physics and Astronomy, University of California, Los Angeles, CA 90095-1562, USA
[3] Institut de Recherche sur les Exoplanètes (iREx), Université de Montréal, Montréal, QC H3C 3J7, Canada
[4] Département de Physique, Université de Montréal, Montréal, QC H3C 3J7, Canada
[5] Center for Astrophysics and Space Sciences, University of California, San Diego, CA 92093-0424, USA
[6] Gemini Observatory/NSF's NOIR Lab, Hilo, HI, 96720, USA
[7] Earth and Planets Laboratory, Carnegie Institution for Science, 5241 Broad Branch Rd NW, Washington, DC 20015, USA

Abstract

We present observations and analyses of eight white dwarf stars (WDs) that have accreted rocky material from their surrounding planetary systems. The spectra of these helium-atmosphere WDs contain detectable optical lines of all four major rock-forming elements (O, Mg, Si, and Fe). This work increases the sample of oxygen-bearing WDs with parent body composition analyses by roughly 33%. To first order, the parent bodies that have been accreted by the eight WDs are similar to those of chondritic meteorites in relative elemental abundances and oxidation states. Seventy-five percent of the WDs in this study have observed oxygen excesses implying volatiles in the parent bodies with abundances similar to those of chondritic meteorites. Three WDs have oxidation states that imply more reduced material than found in CI chondrites, indicating the possible detection of Mercury-like parent bodies, but are less constrained. These results contribute to the recurring conclusion that extrasolar rocky bodies closely resemble those in our solar system, and do not, as a whole, yield unusual or unique compositions.

1. Introduction

Categorization of the compositions of rocky exoplanets, and evaluation of their similarities to or differences from rocky bodies in our solar system, is a challenging and flourishing area of study. To this end, many studies have characterized exoplanet compositions using stellar spectroscopy of FGK, or Sun-like, stars (e.g., Unterborn & Panero 2019; Adibekyan et al. 2021; Kolecki & Wang 2022) in combination with planetary mass–radius relations. An alternative approach is to use white dwarf stars (WDs)—stars in the last stage of stellar evolution—that have been *externally polluted* by accretion of rocky bodies from their surrounding planetary systems. Owing to their strong gravitational acceleration, the atmospheres of WDs are typically devoid of elements heavier than helium. The heavy elements sink out of the observable atmosphere on timescales of days to millions of years (Koester 2009), depending on the atmospheric temperature and dominant constituent (H or He). Because of the relatively short settling timescales of heavy elements, externally polluted WDs must have acquired their heavy elements relatively recently compared to their lifetimes. Radiative levitation as a mechanism to maintain heavy elements in a WD atmosphere (e.g., Chayer et al. 1995) is not effective for the WDs presented herein (helium-atmosphere WDs with effective temperatures cooler than 20,000 K).

WDs for which hydrogen presents the strongest spectral line are referred to as "DAs" and neutral helium as "DBs." If a spectrum displays both H I and He I lines, the spectral type can be either DAB or DBA depending on whether H or He, respectively, has the strongest optical absorption line. WDs are deemed polluted if any element heavier than He is detected in their atmosphere; following Sion et al. (1983) and Wesemael et al. (1993), we denote external pollution with a Z in the spectral classifications.

We now understand that these polluted WDs, constituting 25%–50% of all WDs, accrete material from the planets, asteroids, and comets that orbited the host star and were subsequently scattered toward the star by the post-main-sequence evolution (Debes & Sigurdsson 2002; Jura 2003; Zuckerman et al. 2003, 2010; Koester et al. 2014; Veras 2016). Observations of transiting debris from planetary material that has been tidally disrupted by the WD (Vanderburg et al. 2015; Xu et al. 2016; Vanderbosch et al. 2020; Guidry et al. 2021; Vanderbosch et al. 2021) suggest the presence of a body in the process of being pulverized and accreted by the WD, thus substantiating our understanding of the source of pollution. Analyses of polluted WDs to evaluate the compositions of extrasolar rocky bodies have proliferated in the last decade (e.g., Zuckerman et al. 2007; Klein et al. 2010; Vennes et al. 2010; Farihi et al. 2011; Melis et al. 2011; Zuckerman et al. 2011; Dufour et al. 2012; Gänsicke et al. 2012; Jura et al. 2012; Jura & Young 2014; Xu et al. 2017; Harrison et al. 2018; Hollands et al. 2018; Doyle et al. 2019; Swan et al. 2019; Bonsor et al. 2020; Buchan et al. 2022).

To date, the parent bodies being accreted by polluted WDs mostly resemble dry, rocky bodies similar in size and general composition to asteroids in the solar system. However, a few water-rich bodies (Farihi et al. 2011, 2013; Raddi et al. 2015;

---

[8] Deceased.

Hoskin et al. 2020; Klein et al. 2021), including a Kuiper Belt analog (Xu et al. 2017), have been discovered. Additionally, parent bodies that resemble giant planets (Gänsicke et al. 2019) and icy moons (Doyle et al. 2021) have been argued. While just a few dozen WDs are *heavily* polluted, with more than a few rock-forming elements detected, taken together, 23 distinct elements have been detected in polluted WDs (see Table 1 of Klein et al. 2021). Compositional variations due to igneous differentiation—with compositions that range from crust-like to core-like—have been identified (e.g., Melis et al. 2011; Zuckerman et al. 2011; Gänsicke et al. 2012; Jura & Young 2014; Melis & Dufour 2017; Putirka & Xu 2021; Hollands et al. 2021; Johnson et al. 2022).

In this work, we present new observations of eight heavily polluted DB WDs and examine the compositions of the accreting rocky parent bodies. We focus on evaluating these bodies through bulk composition and oxidation state. In addition to Ca and the four major rock-forming elements (O, Mg, Si, and Fe), instances of additional elements (e.g., Al, Cr, and Ti) have been detected in some of the WDs. These new data increase the sample of oxygen-bearing WDs with parent body composition analyses by ~33%. This paper is organized as follows: in Section 2 we list our target selection and observations for the WDs described. Our atmosphere models are discussed in Section 3 along with spectra of the detected major rock-forming elements. Section 4 provides an analysis of the parent body compositions and in Section 5 we summarize our findings.

2. Observations

2.1. Target Selection

In this paper, we focus on eight DB WDs (Table 1). In each of these WDs, all four major rock-forming elements (O, Mg, Si, and Fe) are detected.

Three out of eight WDs in this work have been observed over the years by members of our team. In particular, we obtained HIRES spectra of WD 1244+498 and SDSS J1248+1005 because they were previously identified as DBZs in Sloan Digital Sky Survey (SDSS) spectra (Kleinman et al. 2013; Koester & Kepler 2015), and WD 1415+234 was followed up at high resolution due to the possible appearance of a Ca II K line as found in Limoges & Bergeron (2010).

The other five WDs were identified in a search for heavily polluted WDs (Melis et al. 2018). We compiled our list of targets by utilizing the sample of probable WDs from Gentile Fusillo et al. (2019), which calculates stellar parameters and the probability of an object being a WD based on fits to Gaia DR2 data.

To focus on finding DB WDs, we compared GALEX colors (Bianchi et al. 2017) to effective temperature (T_{eff}) (Figure 1). Differences in the opacity of DA and DB WDs have a salient effect on emergent fluxes, particularly at UV wavelengths as observed with GALEX. These colors reveal a distinct dichotomy between DA and DB WDs (e.g., Bergeron et al. 2019). We constrained Gaia WD candidates from Gentile Fusillo et al. (2019) to include only those where G mag < 17.0, distance < 300 pc, and far-UV (FUV) and near-UV (NUV) GALEX data exist, (see Figure 1). Known characterizations of each WD are labeled as either green squares (DAs) or blue triangles (DBs), and unconfirmed WD candidates are labeled as gray circles. The polluted DBs analyzed in this paper are represented as red circles.
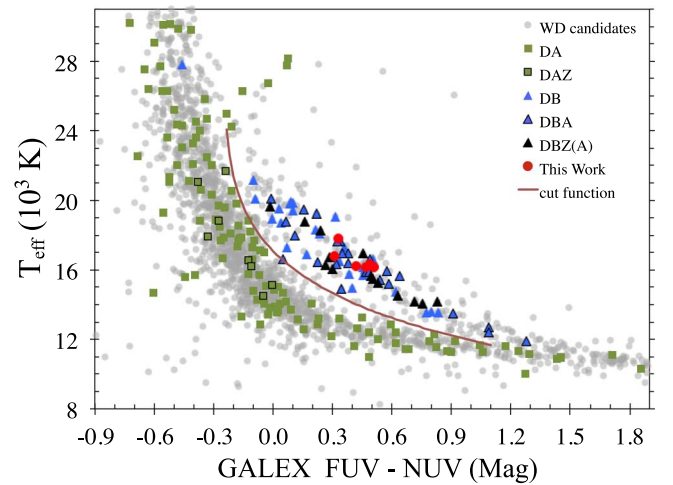

Figure 1. T_{eff} as a function of GALEX colors. Here we show the Gaia WD candidates from Gentile Fusillo et al. (2019) that have both FUV and NUV GALEX data, which reveals a distinct dichotomy between DA and DB WDs. The subset of polluted helium-dominated atmospheres from this work is represented as red-filled circles. The red curve is our constructed *cut function*, which we use to assign likely dominant elements based on the location of the WD parameters on this figure (see also Equation (1)).

To process these data for our purposes, we constructed a cut function (red curve in Figure 1) with the equation

$$T_{eff,cut} = 28,000 \exp\left(-\left(\frac{FUV - NUV + 0.24}{2}\right)^{1/3}\right) \quad (1)$$

that applies for $12,000 < T_{eff} < 24,000$. We used Equation (1) to flag points as *likely DBs* where $T_{eff} > T_{eff,cut}$ (above the red curve in Figure 1) and those where $T_{eff} < T_{eff,cut}$ as *likely DAs* (below the red curve, Figure 1). This allowed us to specifically target WDs that fell within the range of known DBs. This particular selection method for observing WDs led to the discovery of many of the polluted DB WDs in this study, as well as many others to be published in future studies.

2.2. Instrument Setup

Table 1 lists our target WDs along with their observation dates, instruments, and resulting data properties. We describe each instrument and observational setup in more detail below.

2.2.1. KAST

Our large-scale survey to search for heavily polluted WDs from Gaia DR2 WD candidates (described in Section 2.1 and Melis et al. 2018) utilized the KAST Spectrograph on the 3 m Shane telescope at Lick Observatory. Our standard setup implemented the d57 dichroic, which split blue light through the 600/4310 grism and red light through the 830/8460 grating. This setup provides a resolving power ($R = \lambda/\Delta\lambda$) for a 2″ slit in blue and red of $R = 950$ and 1500, respectively, and wavelength coverage from 3450–7800 Å. Where indicated in Table 1, we implemented another version of our setup which tilted the 830/8460 grating to cover redder wavelengths and specifically the Ca infrared triplet (λ 8498/8542/8662 Å) resulting in red arm wavelength coverage from 6440–8750 Å. For both setups, we used slit widths of 1, 1.5, or 2″ and integration times from 45–60 minutes depending on observing

Table 1
WD Observation Data

Name	UT Date	Instrument	Coverage (Å)	Int. Time (s)	S/N[a]
Gaia J0218+3625	2021/08/31	HIRES (blue)	3115–5950	3600	43
	2020/10/08	HIRES (blue)	4000–5950	2000 × 2	7[b, c]
	2019/07/16	HIRES (red)	4715–8995	3300	33
	2018/12/30	Kast	3420–5485, 5590–7840	3300	62
WD 1244+498	2018/05/18	HIRES (blue)	3115–5950	2000	24
	2015/04/09	HIRES (red)	4715–8995	1800 × 2	39[b]
	2010/03/28	HIRES (blue)	3115–5950	3000	25
SDSS J1248+1005	2015/04/09	HIRES (red)	4715–8995	3000 × 2	24[b]
	2014/05/22	HIRES (blue)	3115–5950	3000 × 3	32[b]
WD 1415+234	2019/07/16	HIRES (red)	4715–8995	3300	43
	2016/04/01	HIRES (blue)	3115–5950	2400 × 2	40[b]
	2015/04/25	ESI	3900–10,900	1180 × 2	25[b]
SDSS J1734+6052	2019/09/07	HIRES (red)	4715–8995	3600	29
	2019/07/16	HIRES (red)	4715–8995	3300	34
	2019/07/07	HIRES (blue)	3115–5950	3300	27
	2019/05/29	Kast	3415–5480, 6420–8790	3900	28
Gaia J1922+4709	2020/10/07	HIRES (red)	4715–8995	3600	37
	2020/06/14	HIRES (blue)	3115–5950	3000	28
	2019/12/09	HIRES (red)	4715–8995	3600	26
	2019/10/12	Kast	3420–5485, 6400–8800	3000	42
EC 22211-2525	2021/08/31	HIRES (blue)	3115–5950	3300	40
	2020/10/07	HIRES (red)	4715–8995	3600	46
	2019/07/07	HIRES (blue)	3115–5950	3300	38
	2019/07/03	MagE	3065–9470	1200 × 2	78[b]
	2018/12/12	Kast	3450–5475, 5590–7840	2700	17
SDSS J2248+2632	2019/09/07	HIRES (red)	4715–8995	3300	38
	2019/07/16	HIRES (red)	4715–8995	3300	43
	2019/07/07	HIRES (blue)	3115–5950	3000	36
	2017/12/11	Kast	3430–5500, 5625–7820	3600	62

Notes.
[a] Signal-to-noise-ratio (S/N) measured at 3445 Å for HIRES (blue), 5195 Å for HIRES (red), 5160 Å for MagE, 5100 Å for Kast, and 6000 Å for ESI.
[b] S/N for combined exposures.
[c] Only CCDs 2 and 3 were used in our analysis.

conditions and target brightness. The data were reduced using standard IRAF routines, including bias subtraction, flat fielding, wavelength calibration using arc lamps, and instrumental response calibration using observations of standard stars (Tody 1986). Signal-to-noise ratios (S/Ns) for the resulting spectra are measured at 5100 Å and reported in Table 1.

2.2.2. MagE

Moderate-resolution optical spectra of EC 22211-2525 were acquired with the Magellan Echellette (MagE) spectrograph on the Magellan 1 (Baade) telescope at Las Campanas Observatory on 2019 July 3. EC 22211-2525 was observed through the 0."5 slit providing a resolving power of $R \simeq 7500$. Data reduction was performed with the Carnegie Python pipeline (Kelson et al. 2000; Kelson 2003) and S/N measurements were made at 5160 Å.

2.2.3. ESI

We used the Echellette Spectrograph and Imager (ESI) on the Keck II Telescope at Maunakea Observatory (Sheinis et al. 2002) to obtain a spectrum for WD 1415+234. ESI data were taken with a 0."3 slit providing a resolving power of $R \simeq 13,000$. Data were reduced using MAKEE and IRAF, similar to the HIRES reduction process described in Klein et al.

(2010). S/N for the resulting combined spectrum was ∼25, measured at 6000 Å.

2.2.4. HIRES

We used HIRES on the Keck I Telescope at Maunakea Observatory (Vogt et al. 1994) to obtain higher resolution spectra for each of the eight WDs in this sample. HIRES data were taken with the C5 decker (slit width 1."148) for a resolving power of $R \simeq 37,000$ and resulting in wavelength coverage of 3115–5950 Å with the blue collimator and 4715–8995 Å with the red collimator. Exposure times ranged from 30–60 minutes and depended on observing conditions and target brightness. Data were reduced using either the MAKEE software package with IRAF continuum normalization or IRAF reduction routines (see Klein et al. 2010 for more details on the methods and routines used). The S/N for the resulting spectra were measured at 3445 Å for HIRES blue and 5195 Å for HIRES red, and are displayed in Table 1.

3. Data Analysis

3.1. Spectral Typing

WD spectral types are established according to the appearance of their optical spectra and do not always reflect the dominant atmospheric composition (e.g., GD 16 and GD

Table 2
WD Parameters

WD Name	R.A. (J2000)	Decl. (J2000)	G (mag)	D (pc)	T_{eff} (K)	log g (cgs)	Hα EW (mA)	Hα depth HIRES	Hα depth lowres	CaK EW (mA)	CaK depth HIRES	CaK depth lowres	Spectral Type
Gaia J0218+3625	02 18 16.64	+36 25 07.6	16.4	116	14,700	7.86	475	0.10	0.06	595	0.65	0.13	DBZA
WD 1244+498	12 47 03.28	+49 34 23.5	16.6	120	15,150	7.97	1600	0.26	0.16	664	0.67	0.20	DBAZ
SDSS J1248+1005	12 48 10.23	+10 05 41.2	17.4	164	15,180	8.11	1750	0.28	0.17	1245	0.66	0.39	DBAZ
WD 1415+234	14 17 55.37	+23 11 36.7	16.6	127	17,300	8.17	1150	0.23	0.15	274	0.63	0.07	DBAZ
SDSS J1734+6052	17 34 35.75	+60 52 03.2	16.9	150	16,340	8.04	2000	0.25	0.21	256	0.67	0.08	DBAZ
Gaia J1922+4709	19 22 23.41	+47 09 45.4	16.6	127	15,500	7.95	510	0.16	0.08	528	0.57	0.18	DBZA
EC 22211−2525	22 23 58.39	−25 10 43.6	16.3	109	14,740	7.89	1500	0.24	0.22	710	0.68	0.17	DBAZ
SDSS J2248+2632	22 48 40.93	+26 32 51.6	16.4	123	17,370	8.02	750	0.18	0.15	169	0.55	0.07	DBAZ

Note. G_{mag} and distances (calculated from parallaxes) are from Gaia EDR3 (Gaia Collaboration et al. 2016, 2021). T_{eff} and log g are fit as described in Section 3.2. Typical uncertainties for T_{eff} and log g are ± 500 K and ±0.05, respectively. "lowres" refers to either SDSS or Kast spectra. Line "depth" is the position of the line center between the continuum and zero, measured as the fractional distance below the continuum. Spectral type assignments are based on EWs of Ca II K (CaK) and Hα as described in Section 3.1.

Table 3
Observed Atmospheric Elemental Abundances

Name	$\log(n(\mathrm{H})/n(\mathrm{He}))$	$\log(n(\mathrm{Be})/n(\mathrm{He}))$	$\log(n(\mathrm{O})/n(\mathrm{He}))$	$\log(n(\mathrm{Na})/n(\mathrm{He}))$	$\log(n(\mathrm{Mg})/n(\mathrm{He}))$
Gaia J0218+3625	-6.03 ± 0.15	< -11.0	-5.53 ± 0.15	-7.11 ± 0.15	-6.64 ± 0.15
WD 1244+498	-5.12 ± 0.15	< -11.0	-5.77 ± 0.15	...	-6.79 ± 0.15
SDSS J1248+1005	-5.18 ± 0.15	< -11.0	-5.44 ± 0.15	...	-6.40 ± 0.15
WD 1415+234	-4.92 ± 0.15	< -11.0	-5.59 ± 0.15	...	-5.82 ± 0.17
SDSS J1734+6052	-4.76 ± 0.15	< -10.3	-5.93 ± 0.15	...	-6.62 ± 0.15
Gaia J1922+4709	-5.66 ± 0.15	< -10.4	-5.51 ± 0.15	...	-6.14 ± 0.15
EC 22211−2525	-5.56 ± 0.15	< -11.0	-5.76 ± 0.15	...	-6.52 ± 0.15
SDSS J2248+2632	-5.12 ± 0.15	< -10.5	-5.94 ± 0.15	...	-6.52 ± 0.15

Name	$\log(n(\mathrm{Al})/n(\mathrm{He}))$	$\log(n(\mathrm{Si})/n(\mathrm{He}))$	$\log(n(\mathrm{Ca})/n(\mathrm{He}))$	$\log(n(\mathrm{Ti})/n(\mathrm{He}))$	$\log(n(\mathrm{Cr})/n(\mathrm{He}))$
Gaia J0218+3625	-7.3 ± 0.2	-6.50 ± 0.15	-7.81 ± 0.21	-9.43 ± 0.15	-8.68 ± 0.15
WD 1244+498	...	-6.92 ± 0.15	-7.79 ± 0.17	-9.34 ± 0.15	-8.78 ± 0.16
SDSS J1248+1005	...	-6.65 ± 0.15	-7.22 ± 0.17	-8.80 ± 0.15	-8.41 ± 0.15
WD 1415+234	...	-6.25 ± 0.18	-7.40 ± 0.15	...	-7.81 ± 0.15
SDSS J1734+6052	...	-6.93 ± 0.15	-7.83 ± 0.17	...	...
Gaia J1922+4709	-6.9 ± 0.2	-6.02 ± 0.15	-7.53 ± 0.15	-9.05 ± 0.15	-8.30 ± 0.15
EC 22211−2525	-7.7 ± 0.3	-6.67 ± 0.15	-7.85 ± 0.20	-9.60 ± 0.15	-8.79 ± 0.15
SDSS J2248+2632	...	-6.83 ± 0.15	-7.45 ± 0.23	...	...

Name	$\log(n(\mathrm{Mn})/n(\mathrm{He}))$	$\log(n(\mathrm{Fe})/n(\mathrm{He}))$
Gaia J0218+3625	-8.84 ± 0.15	-6.85 ± 0.15
WD 1244+498	...	-6.58 ± 0.15
SDSS J1248+1005	...	-6.63 ± 0.15
WD 1415+234	...	-5.89 ± 0.15
SDSS J1734+6052	...	-6.85 ± 0.15
Gaia J1922+4709	...	-5.88 ± 0.15
EC 22211-2525	...	-6.84 ± 0.15
SDSS J2248+2632	...	-7.10 ± 0.27

Note. Abundances by number, n, relative to He and uncertainties for each of the WDs in this work. Where statistical uncertainties are small (<0.15 dex), we conservatively set them to 0.15 dex. We have included upper limits on Be abundances, which demonstrate that Be is not detected at the greatly elevated levels seen in two WDs in Klein et al. (2021). We list observed lines used for these abundance determinations in Table A2.

362, Koester et al. 2005; Zuckerman et al. 2007). A colleague prudently pointed out, "Annie Jump Cannon was prophetical when she made it clear that stellar spectral types should never have physical interpretations because she realized models would change but spectral morphology would be static for a given type" (J. Farihi 2022, private communication).

Three stars in our sample (WD 1244+498, SDSS J1248 +1005, WD 1415+234) were previously known WDs; the other five are newly identified in this work. In all cases, as of

the date of this publication, the spectral types in SIMBAD are either absent or need updating.

In trying to determine the appropriate spectral types for this set of WDs, we ran into a matter that requires some clarification. In all these spectra, the He I lines are clearly the dominant optical features: He I $\lambda 5876$ Å equivalent widths (EWs) range from 5–14 Å, and line depths (as defined in Table 2 note) range from 0.34–0.48, with little depth difference between low and high-resolution spectra. Thus the primary

spectral type begins with "DB" in each case (Table 2). However, since each WD also displays Hα and high-Z lines, the question is how to distinguish whether the secondary type should be DBZA or DBAZ? The paradigm established in Sion et al. (1983) and Wesemael et al. (1993) states that the spectral type is defined in order of the *strongest* optical spectral features, but no further definition is given as to what exactly that means. It is ambiguous whether strongest refers to the EW or the line depth. These comparisons can be substantially different depending on the instrument spectral resolution, especially for Ca II $\lambda 3933.663$ Å (CaK), which is typically the high-Z line with the largest EW in our temperature range ($T_{\rm eff}$ < 18,000 K). To illustrate this point, we list the CaK and Hα line depths measured at both higher resolution ($R \sim 37{,}000$) and lower resolution ($R \sim 1000$), as well as their EWs in Table 2.

If all we had were low-resolution spectra, and if we chose to assign secondary spectral types by line depth, then four of the WDs would be DBZA and four DBAZ. But then when those same WDs are observed at high resolution, according to line depth, the four previous DBAZs would all change to DBZAs. Instead, we decided to assign the spectral type according to EW: DBAZ if EW(Hα) > EW(CaK), and DBZA if EW(CaK) > EW(Hα). As long as spectra have sufficient S/N to detect a given line, EW measurements are essentially independent of the instrument resolution, and thus our choice of spectral type should be enduring.

3.2. Stellar Parameters

The effects of additional opacity from the presence of hydrogen and heavier elements in the atmospheres of He-dominated WDs with effective temperatures ($T_{\rm eff}$) < 20,000 K have been well described (Dufour et al. 2007, 2010; Coutu et al. 2019).

We follow an iterative procedure to obtain atmospheric parameters for each target. First, we get a rough estimate for $T_{\rm eff}$ and gravity (log g) by fitting photometry (typically SDSS, but PanSTARRS was used for EC 22211-2525). We then fit the Ca II K (CaK) region and Hα from low-resolution spectra concurrently with SDSS $ugriz$ photometry (Alam et al. 2015) or PanSTARRS $grizy$ photometry (Flewelling et al. 2020) and Gaia parallax (Gaia Collaboration et al. 2016, 2021). Where available (Table 1) we use KAST spectra, otherwise, we use SDSS spectra. Atmospheric structure calculations are then informed by the hydrogen abundance by number, n, (log n(H)/n(He)), and heavy element presence when scaling elements to the number abundance of Ca in a CI chondrite (Lodders 2019).

We compared our fits to Gaia and GALEX photometry to confirm good agreement (see Figure A1); standard de-red-dening corrections were applied as described in Coutu et al. (2019). Our best-fit parameters are given in Table 2. We use these parameters to calculate the model atmospheres from which we produce synthetic spectra for each WD.

3.3. Abundance Measurements

Over a series of multiple iterations, we fit these synthetic spectra to the HIRES data until we find a best-fit abundance solution for each element detected (Table 3). We show a sample of WD spectral lines for detections of O, Mg, Si, Fe, and Ca (Figure 2). In each panel, our spectra are shown in black, and our best-fit model is overlaid in red, and the numerical average abundance is given at the bottom of each panel. Our sample of eight WDs have clear detections of O (7772 Å, multiplet), Mg (4481 Å, multiplet), Si (6347 Å), Fe (5169 Å), and Ca (3933 Å and 8542 Å), as well as other detected lines. Measured radial velocities (RVs) and a full listing of all detected lines with their EWs are given in the Appendix, Tables A1 and A2, respectively. We also discuss some detections of non-photospheric lines in the Appendix and Table A1.

Abundances are reported by number, n, relative to He along with uncertainties for each of the WDs in Table 3. Where elements are detected through multiple lines, we take the average abundance. Uncertainties are measured as the standard deviation where there are multiple lines of the same element. Systematic uncertainties, such as from uncertain atomic data (Vennes et al. 2011; Gänsicke et al. 2012), or other missing physics in atmosphere models (e.g., Klein et al. 2020; Cukanovaite et al. 2021) are difficult to quantify. Therefore, where only one line of an element is observed or where uncertainties are smaller than 0.15 dex, we conservatively set them to 0.15 dex.

4. Discussion

4.1. Accretion and Diffusion

Three phases of accretion and diffusion of planetary debris onto a WD are commonly recognized in the literature: the buildup phase, sometimes referred to as an *increasing* phase, the steady-state phase, and the settling, or *decreasing* phase (e.g., Dupuis et al. 1992, 1993; Koester 2009). Though the specific nomenclature varies, the idea remains the same: as a single parent body accretes onto a WD, the observed pollution will first increase as material accumulates in the WD atmosphere. Then, as material begins to sink through the atmosphere, a steady state is eventually reached between accretion and diffusive settling. Steady state is achieved on a timescale comparable to a few e-folding times for settling. Once the parent body source is depleted, material ceases to accrete, and the observed pollution decreases commensurate with the settling times of the individual elements.

The correction for this effect during steady-state accretion is straightforward—element ratios are multiplied by the inverse ratio of settling timescales; see Equation (7) in Koester (2009) and settling timescales in Table A3.

While it is not clear which accretion state WDs exist in, ongoing accretion can be assumed for WDs with observed infrared excess, which emerge where circumstellar debris disks thermally reprocess the light from the star (Jura 2003). EC 22211-2525 is the only WD in the sample with detected infrared excess (Lai et al. 2021), as can be seen in Figure A1.

4.2. Abundance Pattern

For each of the WDs in this study we compared the observed abundances of rock-forming elements (Mg, Al, Si, Ca, Ti, Cr, and Fe) to those of typical rocky compositions in the solar system (CI chondrite, bulk silicate Earth, and continental crust). In general, the best fit is to CI chondrite. In Figure 3 we illustrate this result using the composition of the parent body polluting WD 1244+498 as an example. The parent body is comparable to CI chondrite, as indicated by the close agreement of chondritic abundances (orange symbols) to the 1:1 line in Figure 3. Indeed, each element agrees with chondritic compositions within a factor of 2.
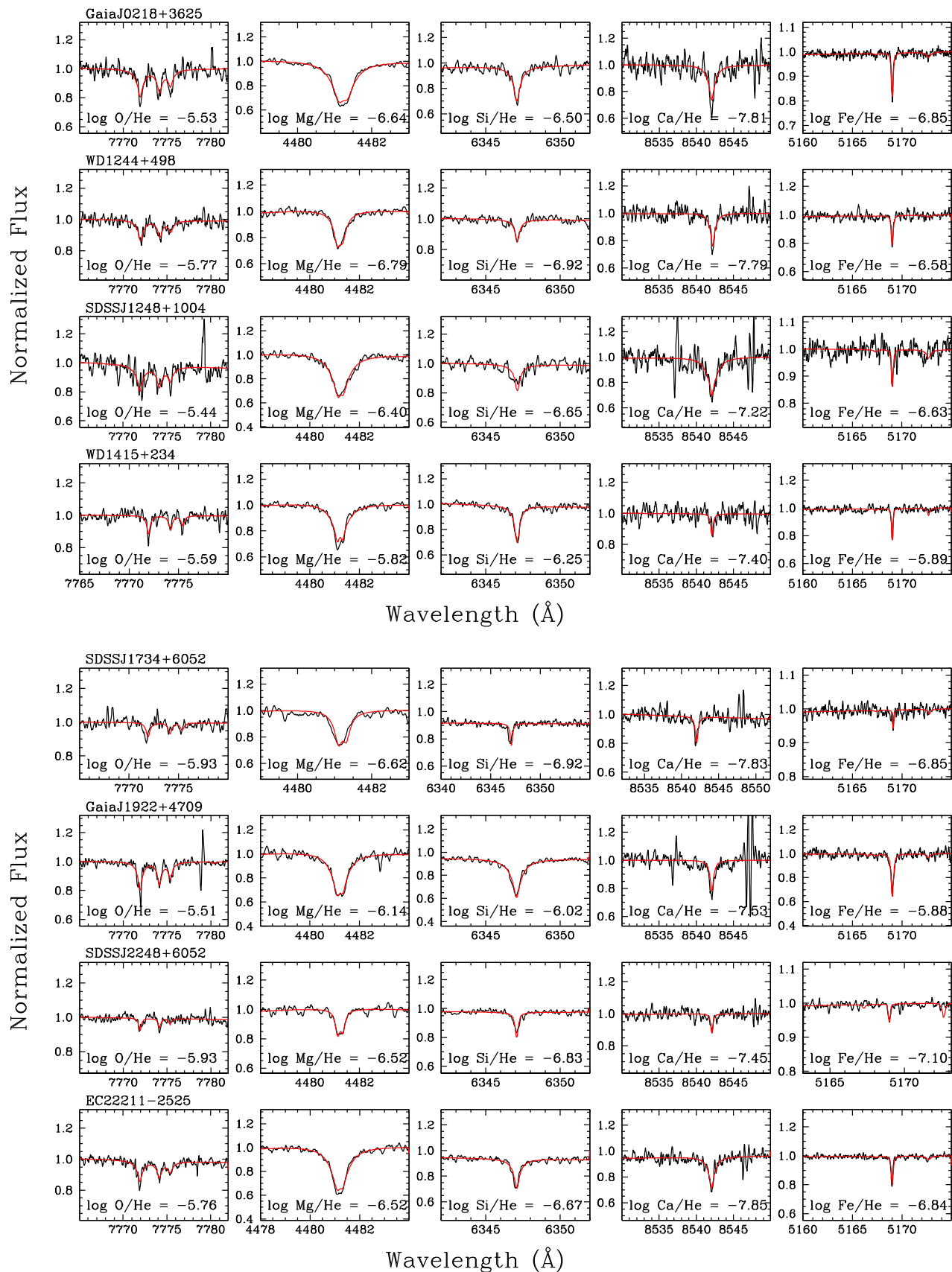
Figure 2. Selected lines for each of the WDs in this study, displaying the detected O triplet and example lines for Mg, Si, Ca, and Fe. Wavelengths are in air and shifted to the laboratory frame of rest. The red line is our best-fit model.

Motivated by Figure 3, we statistically evaluate the hypothesis that the parent bodies being accreted by these eight WDs were approximately chondritic in composition. Similar to Xu et al. (2013); Swan et al. (2019), and Doyle et al. (2021), we compare the goodness of fit for rock-forming elemental abundances observed in each WD to the known composition of CI chondrites using the reduced chi-square statistic, χ_ν^2 (Figure 4). We calculate χ_ν^2 using the elements Al, Si, Ca, Ti, Cr, and Fe, where available for each WD. Oxygen is excluded due to its correlation with the other rock-forming elements (see Section 4.4). Additionally, because we ratio elements to Mg, Mg is not an independent observation for this calculation and is therefore excluded. The data points and their uncertainties shown in Figure 4 represent propagated uncertainties using a Monte Carlo approach with a bootstrap of $n = 1$.

The parameter α represents a probability of obtaining χ_ν^2 values greater than the observed value by chance. Convention suggests that the threshold to reject the hypothesis that the data are consistent with a CI composition is 5% or better, or $\alpha < 0.05$ ($\alpha \sim 0.4$ for $\chi_\nu^2 = 1$). Due to the relatively small number of data points per star, and their uncertainties, the value of χ_ν^2 is also uncertain, which can be accounted for using the approach of Andrae et al. (2010) in which the uncertainty in χ_ν^2 is $\sigma \sim \sqrt{2/N}$ for N data points. Based on a threshold for $\alpha = 0.05$ and a 2σ error for χ_ν^2, we define a critical value, $\chi_{\nu,\mathrm{crit}}^2$, as the reduced chi-square value corresponding to $\alpha = 0.05 + 2\sigma$. Based on these critical values, ranging from 3.5–5.0, depending on the number of elements involved, the relative elemental abundances for the polluted WDs examined here are in good agreement with CI chondrites, with five of the eight WDs having values for χ_ν^2 less than the associated critical values. The remaining WDs have values for χ_ν^2 of 5.08, 7.3, and 4.9, making their fits to CI tentative. For context, we also calculate χ_ν^2 for the bulk Earth, BSE, and terrestrial crustal rocks compared to CI chondrite, where we assume errors equal to the average WD error for each element ratioed to Mg, $n_z/n_{\mathrm{M_g}}$. Note that bulk Earth and BSE are indistinguishable from CI chondrite in this analysis using uncertainties associated with the WD observations of Mg, Al, Si, Ca, Ti, Cr, and Fe. The compositions of continental and oceanic crust, the latter represented by MORB, are readily distinguished from CI chondrite in major elements using WD uncertainties (Figure 4). We see no evidence for crust-like compositions among the eight polluted WDs considered here.

In the examples presented above, we used the observed elemental ratios with no corrections for settling times. This tacitly assumes that the parent body accretion is in the buildup phase. We calculate the same χ_ν^2 statistic to assess the goodness of fit for these WDs relative to the CI elemental ratios assuming the WDs are accreting material in a steady-state phase (Figure 5). Steady state is often assumed for WDs in which heavy element settling times are relatively short. Under this assumption, we find that for three of the eight WDs, the χ_ν^2 values relative to CI chondrite indicate better agreement with CI chondrite than for the buildup-phase assumption. However, with the steady-state assumption, still five of the eight WDs are indistinguishable from CI chondrites ($\chi_\nu^2 < \chi_{\nu,\mathrm{crit}}^2$). Therefore, regardless of whether these polluted WDs are assumed to be in the buildup phase or in steady state, they appear to be accreting bodies that are chondritic, or approximately chondritic, in composition. We note that for Gaia J0218+3625 (irrespective of accretion phase) the abundance of Na/Mg is $\simeq 6\times$ the
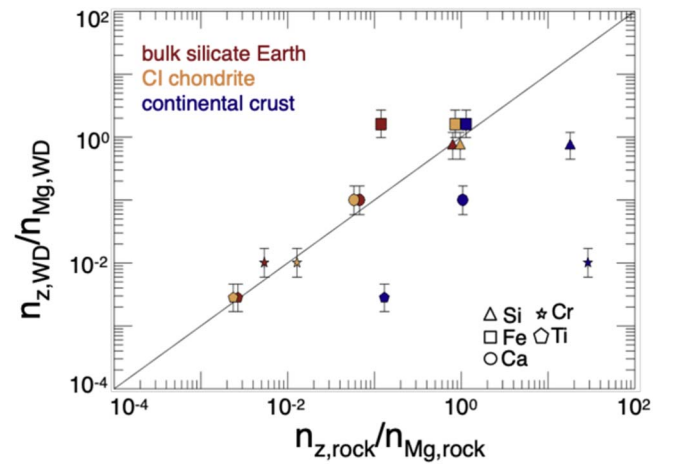

Figure 3. Element/magnesium atomic ratios, z/Mg, for the parent body accreted by WD 1244+498, assuming an increasing phase, relative to z/Mg in various rocks found in our solar system. We compare the calculated parent body elemental abundances accreted by WD 1244+498 to CI chondrite (orange, Lodders 2019), bulk silicate Earth (BSE) (red, McDonough 2003), and the Earth's continental crust (blue, Rudnick 2014). The best match compositionally for the parent body accreting onto WD 1244+498 is CI chondrite.

chondritic ratio. There is likely more work to be done in future analysis of Gaia J0218+3625, but this particular enhanced relative abundance is not sufficient alone to reject the assessment that overall, the accreted bodies of this sample are broadly chondritic.

4.3. Parent Body Size

In order to estimate parent body sizes, we calculate the minimum masses of the parent bodies accreting onto these eight WDs as the sum of the masses of all heavy elements in the convection zone (CVZ). We convert number abundance ratios from Table 3 to mass ratios and multiply by the mass of the CVZ, computed from evolution models from the Montreal White Dwarf Database (MWDD; Dufour et al. 2007).[9] We find minimum masses that range from 2.8×10^{21} to 9.0×10^{22} g. These masses are consistent with some of the most massive asteroids in the solar system ($\sim$8 Flora to 10 Hygiea) and some of the mid-sized moons in the solar system ($\sim$Neptune's Larissa and Saturn's Enceladus). The immensity of these minima for parent body masses supports the conclusion that only the most massive of polluting objects will be observable in WDs (Trierweiler et al. 2022). Mass fluxes onto the WD atmosphere can be obtained by assuming steady state between accretion and settling. For this, we use the CVZ pollution masses and settling times from Table A3. The derived fluxes range from 1.4×10^8 to 8.5×10^9 g s^{-1}, typical for polluted WDs under similar assumptions (e.g., Rafikov 2011; Farihi et al. 2012; Wyatt et al. 2014; Xu et al. 2019) and would result in parent body masses that range from 2.1×10^{21} to 1.4×10^{23} g, assuming accretion from a disk is sustained for roughly 5×10^5 yr (Girven et al. 2012).

4.4. Oxygen and Oxidation State

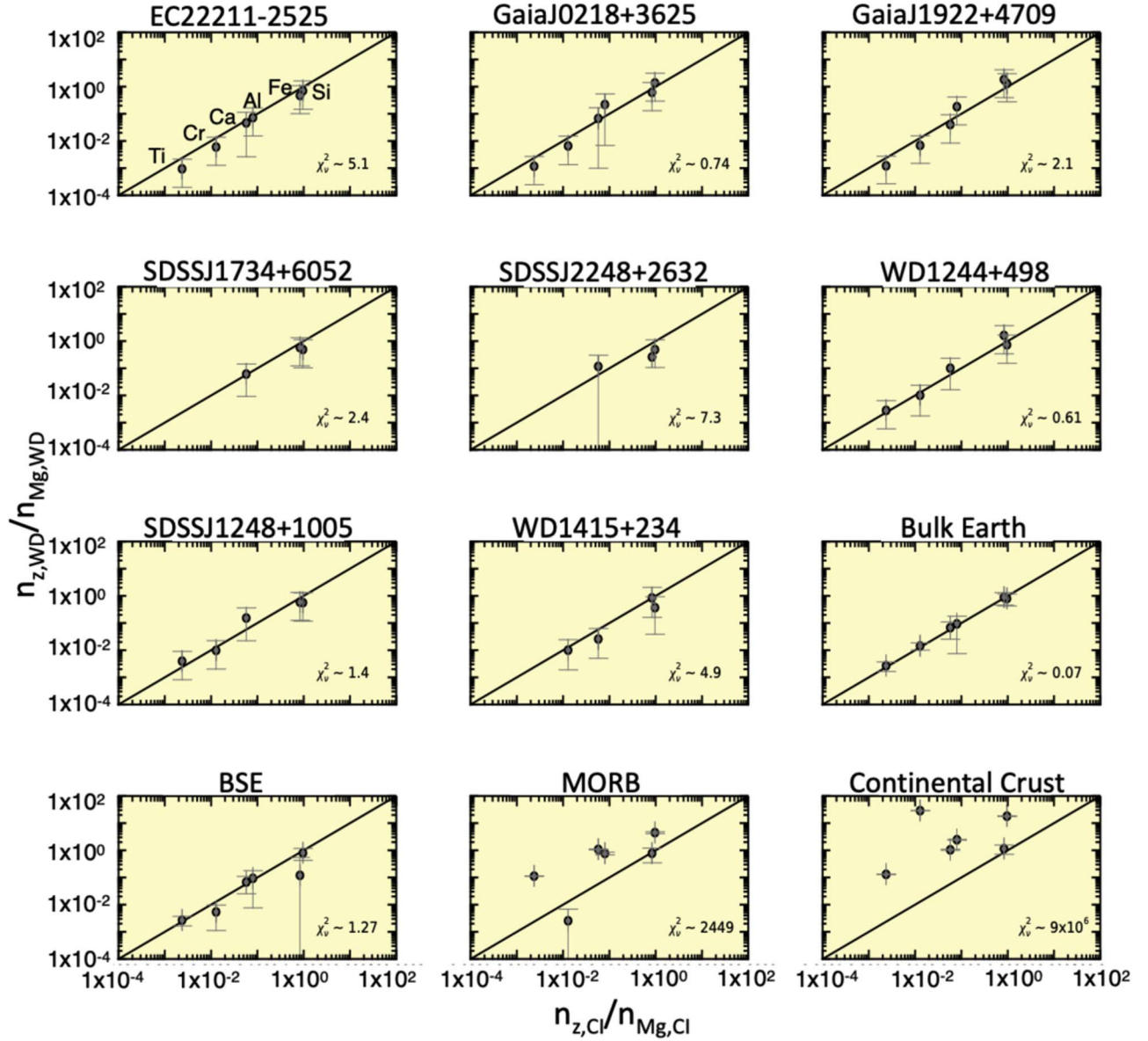We evaluate the oxidation state of the parent bodies accreting onto each WD by following the prescription

---

[9] http://dev.montrealwhitedwarfdatabase.org/evolution.html

Figure 4. One-to-one comparison of major and minor rock-forming elements (n_z), ratioed to Mg (n_{Mg}) and CI chondrite (Lodders 2019) for eight WDs. Abundances are from Table 3, representative of an increasing phase. Errors for WDs are propagated from model abundances and uncertainties using a Monte Carlo approach with a bootstrap of $n = 1$. We report the goodness of fit using a reduced chi-square statistic, χ_ν^2, using the elements Si, Fe, Ca, Al, Cr, and Ti, where available for each WD (see the text), displayed in the bottom right corner of each plot. Generally, the elemental abundances from WD data show good agreement with CI chondrites ($\chi_{\nu,\mathrm{crit.}}^2 <$ 3.5–5.0, depending on which elements are used in the analysis, see the text). For comparison, we calculate χ^2 statistics for known compositions of Earth rocks (bulk Earth (McDonough 2003), bulk silicate Earth (BSE; McDonough 2003), Mid-Ocean Ridge Basalt (MORB; Gale et al. 2013), and the Earth's continental crust (Rudnick 2014)) compared to CI chondrite. Bulk Earth and BSE are in good agreement with CI chondrite, revealing that WD-sized errors in the elements used (Ti, Cr, Ca, Al, Fe, and Si, see Figure 3 and Section 4.2) are unable to distinguish between the two compositions in the data.

introduced by Doyle et al. (2019) and improved in Doyle et al. (2020). We use the ratio of O_{rem}/Fe, where O_{rem} is the O remaining after assigning O to Mg, Si, Ca, and Al to form the oxides MgO, SiO_2, CaO, and Al_2O_3, as an indicator for whether a WD will yield a recoverable oxygen fugacity (ΔIW, see discussion below for complete definition for this parameter) value and error bounds. We calculate O_{rem} relative to Fe as

$$\frac{O_{rem}}{Fe} = \frac{O}{Fe} - \frac{Mg}{Fe} - 2\frac{Si}{Fe} - \frac{3}{2}\frac{Al}{Fe} - \frac{Ca}{Fe}. \qquad (2)$$

For an ideal rock, in which Fe exists as ferrous iron (effective charge of 2+), the value of O_{rem}/Fe should be unity. Where

$O_{rem}/Fe > 1$, an oxygen excess exists, suggesting an additional source for oxygen, often due to accretion of oxygen-bearing volatiles such as H_2O from the parent body (we exclude the effect of Fe^{3+} here, present as the oxide Fe_2O_3, under the assumption that the ferric iron will be relatively minor, $<10\%$ of all Fe, as it is in most solar system rocks). Six of the eight WDs in this study have observed oxygen excesses implying water-rich bodies ($O_{rem}/Fe > 1$; Table 4). Of the six WDs with oxygen excesses, five have an observed amount of H that can account for the excess oxygen assuming a buildup phase. Large abundances of H in helium-dominated WDs are either from primordial H (prior to the DA-to-DB evolution, Rolland et al. 2020)
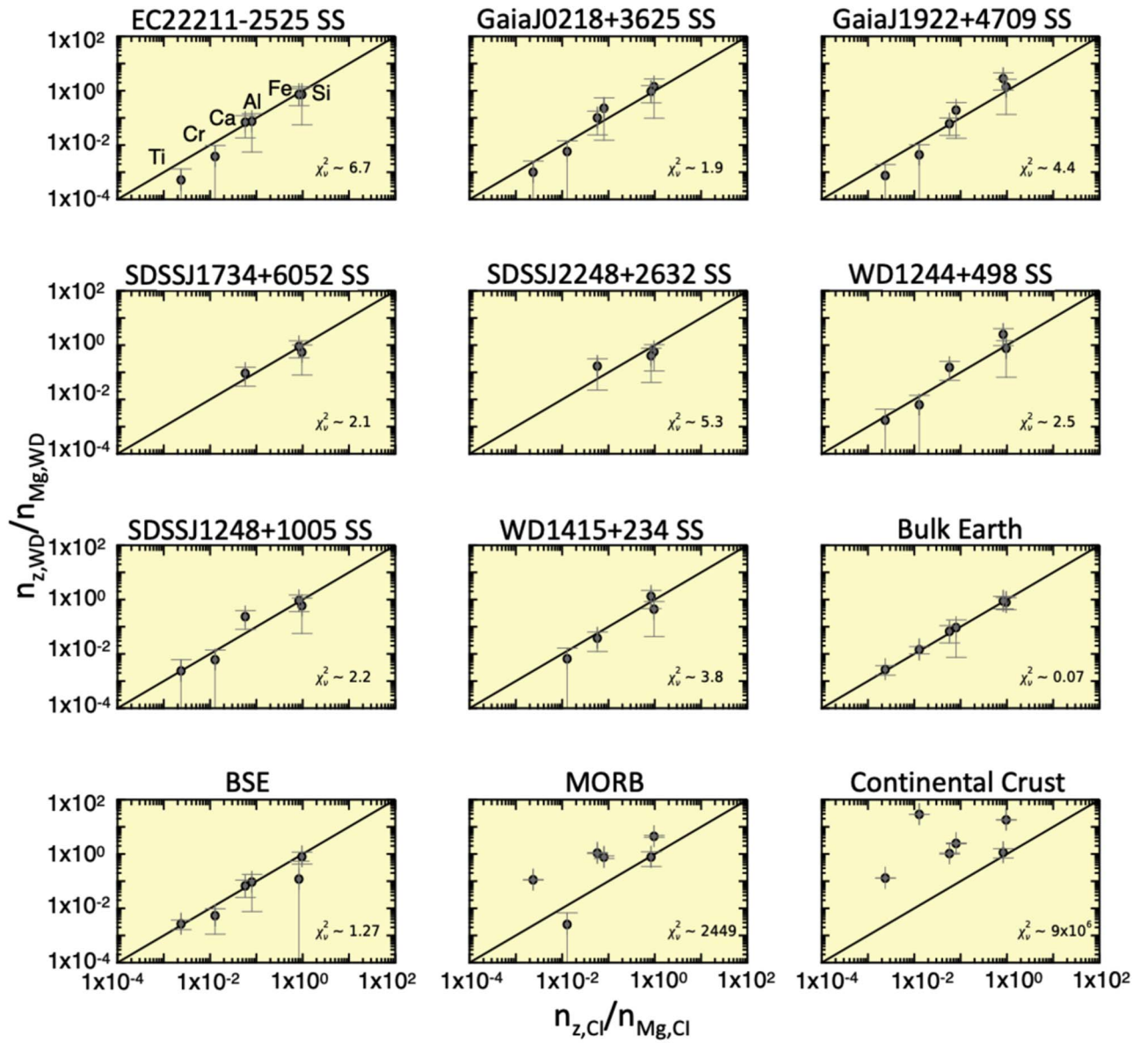
Figure 5. As in Figure 5, but assuming steady-state phase (SS) compositions for the eight WDs presented.

or due to the accumulation of H throughout accretion events, as H floats on the atmospheric surface (Gentile Fusillo et al. 2017; Izquierdo et al. 2021). Notably, a steady-state approximation decreases, but does not entirely remove the oxygen excesses (Table 4).

The level of oxidation in a geochemical system is described as the nonideal partial pressure of O_2, or oxygen fugacity (f_{O_2}), and has implications for the geochemistry and geophysics of rocky bodies. In the planet formation regime, oxygen fugacities are often compared with that defined by the equilibrium reaction between metallic iron (Fe) and FeO, which in mineral form is wüstite (FeO):

$$Fe + \frac{1}{2}O_2 \rightleftharpoons FeO. \qquad (3)$$
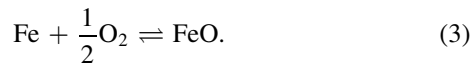
This iron-wüstite (IW) reference reaction assumes pure Fe metal and FeO oxide. By reporting f_{O_2} of a rock to a reference

reaction such as Equation (3), the thermodynamics simplifies to a ratio of activities, or mole fractions (see Appendix in Doyle et al. (2019) for a full derivation). The intrinsic oxygen fugacity of a rock or rocky body can thus be described relative to that for the IW reference, such that

$$\Delta IW \equiv \log\left(f_{O_2}\right)_{rock} - \log\left(f_{O_2}\right)_{IW} = 2\log\left(\frac{x_{FeO}^{rock}}{x_{Fe}^{metal}}\right). \qquad (4)$$

This simplification results in an equation for ΔIW that depends solely on the mole fraction of FeO in the rock (x_{FeO}^{rock}) and the mole fraction of Fe in the metal (x_{Fe}^{metal}).

Where $O_{rem}/Fe < 1$, a dearth of oxygen exists, suggesting iron is present in the form of Fe metal. Of the eight WDs reported in Table 4, three have lower bounds with values for $O_{rem}/Fe < 1$ (WD 1415+234, Gaia J1922+4709, and SDSS J2248+2632). In such cases, lower bounds on the level of oxidation, measured as oxygen fugacity, cannot be obtained.

Table 4
Oxidation States Determined from WD Data in This Study

Name	ΔIW	O_{rem}/Fe	O_{rem}/Fe (steady)
Gaia J0218+3625	$-1.29^{+0.27}_{-0.37}$	$14.16^{+11.02}_{-7.52}$	$9.28^{+8.68}_{-6.68}$
WD 1244+498	$-0.54^{+0.17}_{-0.26}$	$4.69^{+3.53}_{-2.34}$	$3.01^{+2.65}_{-2.03}$
SDSS J1248+1005	$-1.09^{+0.24}_{-0.34}$	$11.23^{+8.58}_{-5.68}$	$7.11^{+6.40}_{-4.90}$
WD 1415+234	< -0.87	$-0.18^{+0.91}_{-0.94}$	$-0.30^{+0.71}_{-0.79}$
SDSS J1734+6052	$-1.04^{+0.26}_{-0.43}$	$4.62^{+4.13}_{-2.97}$	$2.72^{+3.24}_{-2.64}$
Gaia J1922+4709	$-1.78^{+1.17}$	$0.17^{+1.01}_{-0.97}$	$0.03^{+0.89}_{-0.88}$
EC 22211-2525	$-1.25^{+0.28}_{-0.44}$	$6.73^{+6.07}_{-4.36}$	$4.27^{+4.82}_{-3.89}$
SDSS J2248+2632	$-1.74^{+0.49}$	$5.01^{+8.83}_{-5.48}$	$2.44^{+5.77}_{-4.73}$

Note. Calculated ΔIW and remaining O relative to Fe, along with error bounds for the WDs in this study. O_{rem}/Fe for an ideal rock should be unity, and variations from this value are due to oxygen either in excess or shortage of that required to form MgO, SiO$_2$, CaO, and FeO. Measurement uncertainties are propagated using a Monte Carlo approach with a bootstrap of $n = 1$; see Section 4.4 for a discussion about absent lower error bounds for ΔIW. Generally, a steady-state assumption reduces the remaining oxygen, but does not entirely remove the excess, implying that the six WDs with oxygen excesses in the steady-state calculation have some amount of oxygen-bearing volatiles, such as H$_2$O ice, in the parent body.

As in Doyle et al. (2019) and Doyle et al. (2020), we use the oxides SiO$_2$, MgO, FeO, CaO, and Al$_2$O$_3$ to characterize the chemical composition of the accreting rocks. Where Al is not observed, we assume a chondritic Al/Ca ratio and set uncertainties equal to 0.3 dex. Using oxides ensures charge balance and provides a means of tracking oxygen that was in the form of rock. We first assign oxygen to Mg, Si, and Ca to form these oxides, and then we assign the remaining oxygen, O_{rem}, to Fe to form FeO. In this way, we can assess what portion of Fe can be paired with O and is presumed to have existed as FeO in the rock (x^{rock}_{FeO}) versus what portion of Fe existed as Fe metal (i.e., where there is a deficit of O). For application of Equation (4) we set $x^{metal}_{Fe} = 0.85$, consistent with estimates for Fe metal in the core of differentiated bodies from our solar system. We propagate measurement uncertainties for the polluted WDs using a Monte Carlo approach with a bootstrap of $n = 1$. We report our calculated ΔIW values in Table 4.

In our solar system, most rocky bodies are oxidized relative to a hydrogen-rich solar gas ($\Delta IW = -6$), with ΔIW values greater than -3, corresponding to $x^{rock}_{FeO} > 0.025$. Only Mercury and enstatite chondrites are *reduced* ($\Delta IW < -3$; $x^{rock}_{FeO} < 0.025$). In general, the WDs in this study have ΔIW values similar to chondrites, consistent with their chondritic bulk chemistry (Figures 4 and 5). However, there are two WDs in this study for which lower bounds on ΔIW cannot be obtained (Gaia J1922+4709 and SDSS J2248 +2632), and one for which neither a median nor a lower bound can be obtained (WD 1415+234). Situations like these arise where negative x^{rock}_{FeO} values are a significant fraction of the Monte Carlo draws for error propagation. This in turn comes about where there is either a relative scarcity of oxygen relative to the propagated errors or abundance uncertainties are large (refer to Section 2.3 and Figure 3 in Doyle et al. (2020) for a more detailed discussion).

Therefore, the calculation of O_{rem}/Fe is a good indicator of whether a WD will yield a recoverable ΔIW value and error bounds. Indeed, the same three WDs that have lower bounds with negative values for O_{rem}/Fe have unrecoverable lower

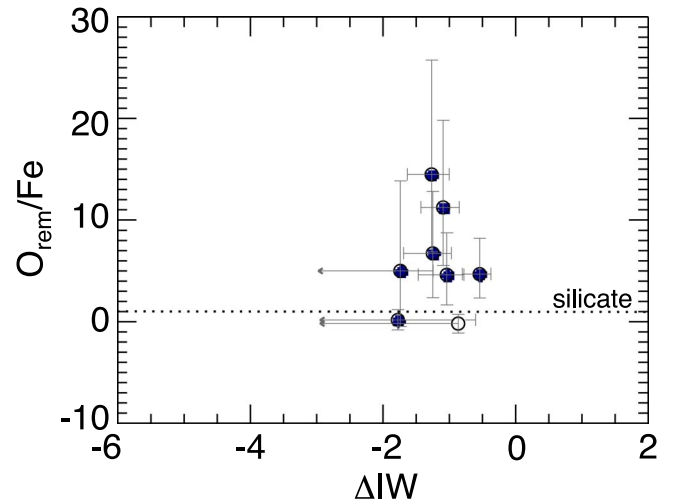**Figure 6.** ΔIW vs. O_{rem}/Fe. The value of O_{rem}/Fe should be unity for ideal rocks, represented as the dotted silicate line. Where $O_{rem}/Fe > 1$, an oxygen excess exists, and where $O_{rem}/Fe < 1$, a dearth of oxygen exists. Where errors allow $O_{rem}/Fe < 1$, lower bounds in ΔIW cannot be obtained. Such is the case for three WDs in this study (Gaia J1922+4709, SDSS J2248+2632, and WD 1415+234). These three WDs are those in the figure where lower error bounds in O_{rem}/Fe plot below the ideal value for silicates. Of these three, WD 1415 +234 is represented with an open circle because the median is also unrecoverable.

error bounds for ΔIW (Figure 6). It is worth noting that one of these WDs, Gaia J1922+4709, is that with the least good fit to CI chondrite, based on χ^2_ν statistics presented in Figure 4. It is also worth noting that one of these WDs, SDSS J2248+2632, has a median value for O_{rem}/Fe that indicates excess oxygen, but large uncertainties for Fe (Table 3). Indeed, it is possible that the parent bodies accreting onto these WDs had less FeO in the rocky portion of the body and were more reduced than CI chondrite. While these WDs have oxidation states that are less constrained, the median values for ΔIW calculated for this subset of polluted WDs generally add to the increasing quantity of chondrite-like parent bodies accreting onto WDs in both bulk composition and degree of oxidation.

5. Conclusions

In this work, we present observations for eight heavily polluted DB WDs and relative elemental abundances for the rocky parent bodies that accreted onto them. All of the WDs in this data set required new designations or updates of spectral types. In a step toward some needed clarification to the spectral classification system, we measured and ordered the *strongest* spectral features according to EWs (not line depths). That determined our assignment of spectral types as DBAZ or DBZA.

We assembled our data set from known polluted DB WDs and by comparing GALEX colors to T_{eff} for WD candidates presented in Gentile Fusillo et al. (2019). This comparison reveals a distinct dichotomy between DA and DB WDs, which we used to target DB WDs to search for those that are heavily polluted. The WDs presented here were chosen due to their detections of all four major rock-forming elements (O, Mg, Si, and Fe). Through this work, we have increased the sample of known oxygen-bearing WDs polluted by rocky parent bodies by ~33%.

We assessed the bulk compositions and oxidation states of the accreting bodies, and find that they are indistinguishable

from chondritic in composition. This adds to the growing body of evidence suggesting that extrasolar rocky bodies closely resemble those in our solar system, and do not, as a whole, yield unusual or unique compositions. This result is not dependent on assumptions of an increasing phase versus a steady-state phase of accretion.

Six of the eight WDs in this study have observed oxygen excesses implying volatiles, in various abundances, in the parent bodies (a trait shared by CI chondrites). Generally, the oxidation states of these parent bodies also corroborate the conclusion that the accreting bodies are chondritic. Three exceptions exist in which oxidation states are less constrained and could be more reduced than chondritic (lower oxygen fugacity values), and one of these WDs (Gaia J1922+4709) is the same WD that obtains the least good fit to CI chondrite. This result is in accordance with the assessment that perhaps 1/4 of polluted WDs may be consistent with more reduced parent bodies that cannot be identified by use of this method (Doyle et al. 2020). Overall, our results are consistent with the emerging view that extrasolar rocks across the solar neighborhood are broadly similar to rocky bodies in our solar system.

Appendix

This appendix presents details of spectral line measurements, broadband spectral energy distributions (SEDs), diffusion timescales, and accretion rates. RVs are given in Table A1, EWs are given in Table A2, SEDs are displayed in Figure A1, and accretion-diffusion data are reported in Table A3. EWs were measured by profile fitting using IRAF's *splot* task, and RVs were calculated as Doppler shifts of the measured line centers relative to laboratory wavelengths (see Klein et al. 2021).

Half of the stars in this sample (WD 1415+234, SDSS J1734 +6052, Gaia J1922+4709, and SDSS J2248+2632) display absorption lines of the Na I resonance doublet $\lambda5889.951/5895.924$ Å (NaD) with RVs that are significantly blueshifted from the photospheric averages based on many photospheric lines (see Table A1). In some stars, non-photospheric Ca II $\lambda3933.663$ Å (CaK) features are also observed. Based on results from Redfield & Linsky (2008) and Welsh et al. (2010), it is probably the case that WD 1415+234, SDSS J1734+6052, and Gaia J1922+4709 host interstellar medium (ISM) features.

On the other hand, if the non-photospheric RV is blueshifted from the photospheric RV by an amount equal to or somewhat less than the gravitational redshift of the WD, then it could be that the non-photospheric absorption is occurring in CS gas (comoving with the WD, but not fully in its photospheric gravitational well). Referring to Table A1, and considering an uncertainty range of 3 km s^{-1} in gravitational redshift plus 2 km s^{-1} in photospheric RV, a CS origin is reasonable for only two WDs: SDSS J1734+6052 and SDSS J2248+2632. However, we cannot rule out the possibility that absorption may be due to ISM material (especially at distances > 80 pc; e.g., see Figure 7 of Welsh et al. 2010) or could even possibly have some association with accretion-related outflows.

Unlike the four aforementioned WDs, the NaD RV in Gaia J0218+3625 agrees exactly with the average photospheric RV. There may be a slight chance that an ISM cloud has the unusually high RV of 39 km s^{-1} (e.g., Redfield & Linsky 2008 and Welsh et al. 2010) and is coincidentally the same as the WD RV. We think this unlikely, and deem the Na line in Gaia J0218+3625 to originate in the WD photosphere and be associated with the polluting parent body.

Table A1
RVs

WD Name	D	Photospheric Lines			Systemic RV	Additional Lines				Vel Diff from Phot	Grav Red-Shift	Origin of Extra Lines
	(pc)	# of Lines	Avg RV (km s^{-1})	Std Dev (km s^{-1})	(km s^{-1})	NaD$_2$ EW (mÅ)	NaD$_2$ RV (km s^{-1})	CaK EW (mÅ)	CaK RV (km s^{-1})	(km s^{-1})	(km s^{-1})	
Gaia J0218+3625	116	83	39.5	1.6	16.1	45	39.2	...	...	0.2	23.4	Phot
WD 1244+498	120	46	39.1	2.5	11.1	...	...	...	...	...	28.0	...
SDSS J1248+1005	164	62	41.0	1.9	5.6	...	...	...	...	...	35.4	...
WD 1415+234	127	57	34.1	1.5	−4.7	36	−15.8	...	...	49.9	38.8	ISM
SDSS J1734+6052	150	25	17.7	1.9	−13.9	69	−31.3	9	−28.1	47.8	31.6	ISM
	...	...	...	...	...	60	−21.1	7	−18.7	38.2	31.6	ISM or CS?
Gaia J1922+4709	127	104	44.8	1.4	17.7	33	−22.6	...	...	67.8	27.1	ISM
	...	...	...	...	...	...	...	37	−16.1	60.9	27.1	ISM
EC 22211-2525	109	88	47.1	1.6	22.6	...	...	...	...	...	24.5	...
SDSS J2248+2632	123	16	21.2	1.6	−9.4	54	−9.1	...	...	29.9	30.6	ISM or CS?

Note. RVs are in the heliocentric frame of rest. "Avg" RV is the average of the set of observed high-Z line RVs (includes gravitational redshift); "Std Dev" is the standard deviation of that set, which can be taken to be a measure of the uncertainty on the average; "systemic" RV is the kinematic portion of the RV (gravitational redshift subtracted); "Vel Diff from Phot" = Avg RV—NaD and/or CaK RV; "Phot" = photosphere. CaK measurements in this table are of secondary features associated with the CaK wavelength (3933.663 Å in air) that are velocity shifted from the photospheric CaK lines (reported in Table A2). NaD$_2$ = λ5889.951 Å, the stronger line of the Na I resonance doublet. SDSS J1734+6052 has two distinct absorption lines at each of the two NaD doublet transitions, as well as at CaK. Gravitational redshifts are from the MWDD (Dufour et al. 2017 (https://www.montrealwhitedwarfdatabase.org/evolution.html)), calculated with atmospheric parameters from Table 2. Typical EW uncertainties are ~10%–20%. The typical uncertainty for gravitational redshift is 3 km s^{-1} as realized by propagating from the upper and lower bounds of the $T_{\rm eff}$/log g uncertainties from Table 2. Systemic RV uncertainties can be calculated as an additive combination (in quadrature) of the 3 km s^{-1} from gravitational redshift with the standard deviation of photospheric lines.

Table A2
Photospheric Absorption Line Measurements

WD		0218+3625	22,211−2525	1244+498	1248+1005	1922+4709	1734+6052	1415+234	2248+2632
$T_{\rm eff}$		14,700 K	14,740 K	15,150 K	15,180 K	15,500 K	16,340 K	17,300 K	17,370 K
Ion	λ (Å)	EW (mÅ)							
O I	7771.944	200 (27)	134 (15)	138 (22)	266 (59)	152 (13)	93 (22)	80 (11)	43 (18)
O I	7774.166	129 (30)	88 (16)	109 (26)	106 (28)	124 (15)	31 (27)	35 (9)	31 (13)
O I	7775.388	100 (19)	81 (19)	55 (33)	71 (21)	82 (12)	19 (7)	29 (10)	...
O I	8446.359	149 (57)	167 (33)	75 (22)	395 (141)	134 (26)	...	63 (34)	...
Na I	5889.951	45 (10)	...	...	...	...	...	...	...
Mg I	3829.355	...	11 (3)	...	...	...	...	...	...
Mg I	3832.304	31 (5)	42 (3)	15 (5)	43 (8)	39 (6)	...	11 (3)	...
Mg I	3838.292	58 (4)	74 (3)	65 (8)	76 (16)	73 (7)	...	47 (7)	...
Mg I	5172.684	...	9 (2)	...	...	15 (4)	...	...	...
Mg I	5183.604	17 (3)	31 (4)	...	...	32 (10)	...	...	...
Mg II	4481[a]	321 (11)	400 (8)	216 (11)	368 (42)	374 (25)	160 (15)	276 (8)	97 (13)
Mg II	7877.054	...	208 (64)	...	179 (68)	366 (49)	...	91 (41)	...
Mg II	7896.366	309 (72)	337 (51)	...	230 (82)	473 (40)	...	195 (41)	104 (36)
Al II	3587[a]	163 (25)	39 (14)	...	...	241 (45)	...	...	...
Si II	3853.665	19 (4)	14 (3)	...	...	35 (6)	8 (4)	11 (4)	...
Si II	3856.018	105 (3)	83 (5)	54 (6)	72 (5)	186 (6)	33 (5)	82 (3)	30 (6)
Si II	3862.595	70 (2)	48 (4)	19 (4)	46 (5)	128 (8)	21 (4)	58 (3)	20 (3)
Si II	4128.054	59 (3)	36 (5)	13 (5)	25 (7)	133 (13)	13 (4)	39 (5)	...
Si II	4130.894	92 (3)	56 (4)	35 (5)	80 (13)	192 (12)	21 (4)	58 (5)	...
Si II	5041.024	41 (8)	28 (9)	...	...	152 (13)	...	36 (7)	...
Si II	5055.984	85 (6)	58 (12)	30 (8)	114 (17)	203 (27)	27 (8)	54 (8)	...
Si II	5957.559	...	...	...	...	27 (7)	...	...	...
Si II	5978.930	...	...	...	...	81 (13)	...	...	...
Si II	6347.109	232 (14)	200 (16)	104 (10)	217 (37)	413 (13)	126 (37)	186 (12)	97 (7)
Si II	6371.371	153 (12)	103 (12)	46 (7)	158 (29)	255 (10)	63 (7)	89 (11)	50 (6)
Ca II	3158.869	158 (7)	136 (8)	128 (8)	255 (12)	187 (11)	54 (7)	77 (7)	26 (5)
Ca II	3179.331	175 (15)	181 (10)	154 (13)	379 (15)	246 (22)	82 (15)	93 (8)	47 (6)
Ca II	3181.275	52 (6)	43 (9)	...	41 (7)	52 (13)	6 (3)	...	...
Ca II	3706.024	39 (12)	31 (4)	...	87 (8)	66 (8)	...	9 (2)	...
Ca II	3736.902	86 (3)	86 (3)	93 (6)	160 (6)	137 (10)	19 (4)	27 (3)	...
Ca II	3933.663	595 (20)	710 (11)	664 (33)	1245 (38)	528 (23)	256 (8)	274 (4)	169 (7)
Ca II	3968.469	338 (15)	391 (13)	430 (59)	747 (50)	284 (17)	149 (3)	154 (4)	111 (4)

Table A2
(Continued)

WD T_{eff}		0218+3625 14,700 K	22,211−2525 14,740 K	1244+498 15,150 K	1248+1005 15,180 K	1922+4709 15,500 K	1734+6052 16,340 K	1415+234 17,300 K	2248+2632 17,370 K
Ca II	8498.023	…	…	…	173 (53)	…	…	…	…
Ca II	8542.091	305 (61)	305 (40)	228 (24)	528 (57)	255 (18)	120 (17)	60 (26)	88 (31)
Ca II	8662.141	192 (50)	193 (27)	175 (24)	386 (52)	96 (16)	53 (16)	45 (12)	…
Ti II	3168.518	…	…	…	…	…	…	…	…
Ti II	3234.520	20 (2)	15 (2)	…	45 (8)	…	…	…	…
Ti II	3236.578	16 (3)	10 (2)	…	40 (7)	…	…	…	…
Ti II	3239.044	…	11 (3)	…	34 (7)	…	…	…	…
Ti II	3241.994	9 (2)	9 (2)	…	18 (4)	…	…	…	…
Ti II	3248.598	…	…	…	16 (7)	…	…	…	…
Ti II	3322.941	…	…	…	35 (7)	…	…	…	…
Ti II	3341.880	16 (3)	8 (3)	…	36 (4)	…	…	…	…
Ti II	3349.037	13 (2)	8 (2)	14 (9)	47 (11)	26 (5)	…	…	…
Ti II	3349.408	36 (3)	26 (2)	19 (4)	56 (6)	48 (7)	…	…	…
Ti II	3361.218	17 (3)	13 (2)	…	48 (4)	…	…	…	…
Ti II	3372.800	16 (22)	11 (2)	…	30 (3)	…	…	…	…
Ti II	3383.768	12 (4)	11 (2)	…	29 (4)	…	…	…	…
Ti II	3387.846	…	…	…	34 (13)	…	…	…	…
Ti II	3685.189	17 (6)	14 (4)	…	29 (5)	…	…	…	…
Ti II	3759.296	11 (2)	6.3 (1.6)	…	16 (3)	…	…	…	…
Ti II	3761.323	6 (1)	6.1 (1.3)	…	13 (3)	…	…	…	…
Cr II	3118.646	13 (4)	18 (4)	…	31 (8)	19 (6)	…	12 (3)	…
Cr II	3120.359	28 (5)	30 (4)	…	31 (7)	38 (9)	…	12 (2)	…
Cr II	3124.973	32 (5)	37 (4)	27 (6)	43 (9)	40 (11)	…	27 (6)	…
Cr II	3132.053	40 (5)	44 (4)	28 (5)	53 (7)	65 (9)	…	32 (3)	…
Cr II	3147.220	…	9 (3)	…	14 (4)	…	…	…	…
Cr II	3180.693	18 (4)	16 (4)	…	…	…	…	…	…
Cr II	3197.075	8 (3)	8 (3)	…	…	…	…	…	…
Cr II	3368.041	19 (2)	15 (2)	…	22 (3)	28 (7)	…	12 (3)	…
Cr II	3408.757	15 (3)	13 (2)	…	…	…	…	9 (2)	…
Cr II	3422.732	13 (2)	…	…	…	…	…	…	…
Cr II	3433.295	9 (2)	…	…	…	…	…	…	…
Mn II	3441.988	17 (2)	…	…	…	…	…	…	…
Mn II	3460.316	15 (3)	…	…	…	…	…	…	…
Fe I	3570.097	…	…	…	…	25 (7)	…	…	…
Fe I	3581.195	7 (2)	…	…	…	34 (5)	…	…	…
Fe I	3734.864	5 (2)	…	…	…	25 (5)	…	…	…
Fe I	3749.485	…	…	…	…	17 (5)	…	…	…
Fe II	3135.360	…	25 (4)	…	…	54 (9)	…	16 (3)	…
Fe II	3144.752	…	10 (3)	…	…	23 (8)	…	…	…
Fe II	3154.202	44 (4)	61 (5)	67 (17)	62 (10)	79 (10)	9 (4)	40 (3)	…
Fe II	3162.798	…	11 (3)	…	…	40 (6)	…	…	…
Fe II	3167.857	36 (7)	23 (2)	37 (14)	20 (4)	77 (9)	…	32 (4)	…
Fe II	3170.337	…	…	…	…	24 (6)	…	…	…
Fe II	3177.532	22 (6)	17 (3)	17 (4)	…	56 (8)	…	34 (6)	…
Fe II	3180.149	…	…	…	…	27 (6)	…	…	…
Fe II	3183.111	15 (4)	16 (5)	…	…	38 (7)	…	10 (3)	…
Fe II	3186.737	16 (4)	21 (5)	23 (5)	…	44 (9)	…	14 (4)	…
Fe II	3192.909	19 (4)	15 (3)	12 (3)	…	45 (9)	…	12 (2)	…
Fe II	3193.799	42 (6)	32 (4)	35 (5)	44 (8)	79 (7)	…	34 (4)	…
Fe II	3196.070	18 (3)	24 (3)	17 (3)	27 (6)	62 (15)	…	14 (3)	…
Fe II	3210.444	28 (4)	39 (4)	29 (5)	38 (6)	78 (9)	…	27 (3)	…
Fe II	3212.017	…	8 (3)	…	…	41 (8)	…	…	…
Fe II	3213.309	55 (4)	68 (3)	52 (4)	41 (4)	104 (15)	17 (4)	39 (3)	9 (3)
Fe II	3227.742	69 (6)	84 (4)	97 (5)	95 (9)	151 (7)	26 (5)	60 (7)	16 (5)
Fe II	3231.706	…	…	…	…	24 (5)	…	…	…
Fe II	3232.785	8 (2)	8 (2)	17 (4)	…	20 (6)	…	10 (3)	…
Fe II	3237.399	…	…	…	…	30 (9)	…	…	…
Fe II	3237.820	10 (3)	7 (2)	…	16 (6)	32 (7)	…	7 (2)	…
Fe II	3243.723	11 (5)	12 (2)	16 (4)	…	35 (6)	…	9 (3)	…
Fe II	3247.175	27 (4)	15 (3)	28 (6)	17 (4)	75 (8)	…	18 (2)	…
Fe II	3255.887	10 (2)	11 (2)	…	…	37 (6)	…	13 (2)	…
Fe II	3258.771	12 (2)	20 (2)	10 (3)	18 (5)	45 (6)	…	21 (4)	…
Fe II	3259.051	24 (3)	19 (2)	20 (4)	22 (5)	68 (8)	…	24 (5)	…

Table A2
(Continued)

WD $T_{\rm eff}$		0218+3625 14,700 K	22,211−2525 14,740 K	1244+498 15,150 K	1248+1005 15,180 K	1922+4709 15,500 K	1734+6052 16,340 K	1415+234 17,300 K	2248+2632 17,370 K
Fe II	3276.604	…	…	…	…	20 (5)	…	…	…
Fe II	3277.348	13 (2)	13 (2)	…	…	30 (5)	…	9 (2)	…
Fe II	3281.292	…	…	…	…	19 (5)	…	…	…
Fe II	3289.354	…	…	…	…	28 (5)	…	…	…
Fe II	3323.063	…	9 (3)	…	…	36 (8)	…	…	…
Fe II	3468.678	…	…	…	…	30 (4)	…	…	…
Fe II	3493.470	11 (3)	12 (2)	…	…	37 (6)	…	14 (2)	…
Fe II	3748.483	…	…	…	…	24 (6)	…	…	…
Fe II	4233.170	12 (2)	11 (3)	…	…	42 (5)	…	10 (3)	…
Fe II	4351.769	…	…	…	…	23 (6)	…	…	…
Fe II	4522.634	…	…	…	…	19 (5)	…	…	…
Fe II	4549.474	…	…	…	…	54 (11)	…	…	…
Fe II	4583.837	13 (2)	…	…	…	50 (7)	…	…	…
Fe II	4923.927	23 (10)	47 (16)	29 (13)	32 (11)	40 (11)	9 (3)	13 (3)	…
Fe II	5001.959	…	…	…	…	32 (10)	…	…	…
Fe II	5018.440	27 (5)	31 (11)	34 (7)	37 (8)	68 (10)	11 (4)	31 (6)	…
Fe II	5035.708	…	…	…	…	16 (5)	…	…	…
Fe II	5100.727	…	…	…	…	40 (6)	…	…	…
Fe II	5169.033	45 (3)	56 (6)	53 (7)	47 (7)	143 (12)	13 (4)	47 (5)	8 (2)
Fe II	5197.577	…	…	…	…	19 (4)	…	…	…
Fe II	5216.863	…	…	…	…	21 (7)	…	…	…
Fe II	5227.481	…	…	…	…	78 (10)	…	…	…
Fe II	5234.625	…	…	…	…	24 (3)	…	…	…
Fe II	5247.952	…	…	…	…	19 (6)	…	…	…
Fe II	5251.233	…	…	…	…	21 (7)	…	…	…
Fe II	5260.259	…	…	…	…	86 (10)	…	…	…
Fe II	5276.002	…	…	…	…	23 (4)	…	…	…
Fe II	5291.666	…	…	…	…	21 (5)	…	…	…
Fe II	5316.615	15 (3)	…	18 (7)	…	51 (6)	…	…	…
Fe II	5339.585	…	…	…	…	47 (16)	…	…	…
Fe II	5362.869	…	…	…	…	17 (3)	…	…	…
Fe II	5506.195	…	…	…	…	45 (11)	…	…	…

Note. Wavelengths are in air. EW measurements and uncertainty estimates were made using IRAF's task *splot* as described in Klein et al. (2021).
[a] Blended multiplet—the EW is the total for the blended feature.

Table A3
Diffusion Timescales and Accretion Rates for WDs in This Study

Name	τ_{Al} Myr	τ_{Ca}	τ_{Mg}	τ_{Si}	τ_{Fe}	τ_{O}	τ_{Na}	τ_{Ti}	τ_{Cr}	τ_{Mn}
Gaia J0218+3625	1.71	1.19	1.77	1.73	1.16	1.77	1.70	1.09	1.12	1.12
WD 1244+498	0.86	0.60	0.90	0.87	0.59	0.90	...	0.55	0.57	...
SDSS J1248+1005	0.47	0.32	0.49	0.47	0.31	0.48	...	0.29	0.30	0.30
WD 1415+234	0.11	0.09	0.13	0.11	0.08	0.13	...	...	0.08	...
SDSS J1734+6052	0.35	0.25	0.37	0.33	0.24	0.38	...	...	...	...
Gaia J1922+4709	0.77	0.53	0.81	0.76	0.53	0.81	...	0.50	0.51	0.51
EC 22211-2525	1.42	0.98	1.47	1.43	0.96	1.47	...	...	...	...
SDSS J2248+2632	0.19	0.15	0.21	0.18	0.14	0.23	...	...	...	...

Name	M_{CV} g	$\dot{M}_{Al}$ g s^{-1}	$\dot{M}_{Ca}$	$\dot{M}_{Mg}$	$\dot{M}_{Si}$	$\dot{M}_{Fe}$	$\dot{M}_{O}$	$\dot{M}_{Na}$	$\dot{M}_{Ti}$	$\dot{M}_{Cr}$	$\dot{M}_{Mn}$
Gaia J0218+3625	4.4×10^{27}	2.77×10^{7}	1.83×10^{7}	1.10×10^{8}	1.79×10^{8}	2.40×10^{8}	9.34×10^{8}	3.72×10^{7}	5.77×10^{5}	3.39×10^{6}	2.50×10^{6}
WD 1244+498	2.3×10^{27}	5.86×10^{7} [a]	8.15×10^{7}	3.42×10^{8}	3.42×10^{8}	1.98×10^{9}	2.22×10^{9}	...	2.89×10^{6}	1.12×10^{7}	...
SDSS J1248+1005	1.4×10^{27}	2.21×10^{8} [a]	3.14×10^{8}	8.46×10^{8}	6.60×10^{8}	1.79×10^{9}	4.89×10^{9}	...	1.03×10^{7}	2.71×10^{7}	2.56×10^{6}
WD 1415+234	2.6×10^{26}	1.68×10^{7} [a]	2.35×10^{7}	3.83×10^{8}	1.93×10^{8}	1.15×10^{9}	3.97×10^{8}	...	...	1.24×10^{7}	...
SDSS J1734+6052	3.7×10^{26}	2.23×10^{6} [a]	2.89×10^{6}	1.90×10^{7}	1.12×10^{7}	3.89×10^{7}	6.07×10^{7}	...	...	...	...
Gaia J1922+4709	1.9×10^{27}	7.01×10^{7}	3.31×10^{7}	3.29×10^{8}	5.29×10^{8}	2.13×10^{9}	9.14×10^{8}	...	1.29×10^{6}	7.65×10^{6}	3.98×10^{6}
EC 22211-2525	3.8×10^{27}	1.25×10^{7}	1.73×10^{7}	1.51×10^{8}	1.27×10^{8}	2.53×10^{8}	5.74×10^{8}	...	4.07×10^{5}	2.73×10^{6}	1.21×10^{6}
SDSS J2248+2632	3.8×10^{26}	9.05×10^{6} [a]	1.34×10^{7}	4.50×10^{7}	2.66×10^{7}	4.22×10^{7}	1.14×10^{8}	...	...	...	...

Note. Diffusion timescales are from the MWDD (Dufour et al. 2017). Mass fluxes are calculated as described in Section 4.3 for the steady-state accretion phase. M_{CV} is the convection zone mass.
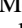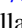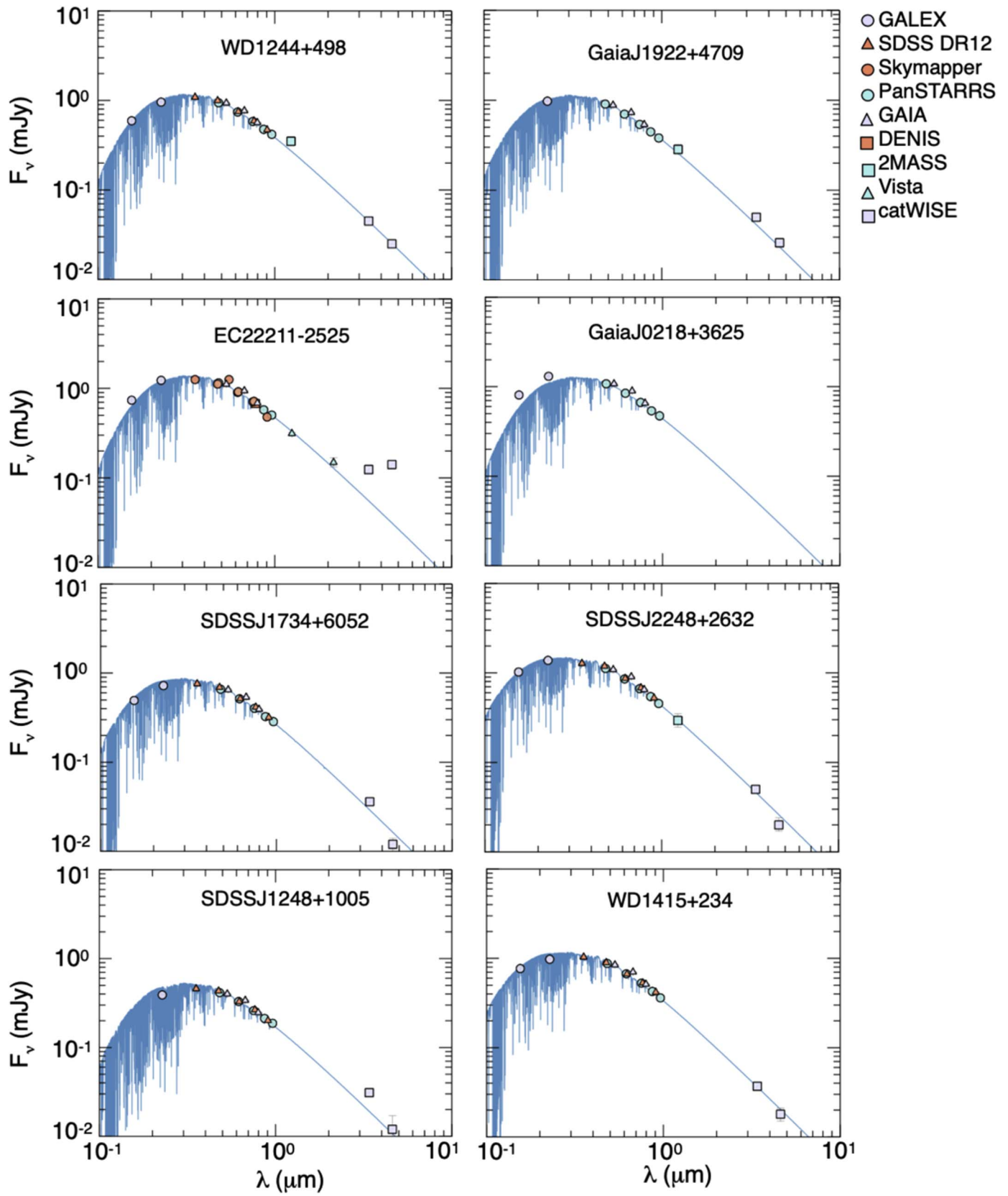[a] Al abundance approximated from a chondritic Al/Ca ratio.

Figure A1. SEDs for the eight DB WDs in this study.

ORCID iDs

Alexandra E. Doyle ⓘ https://orcid.org/0000-0003-0053-3854
Beth L. Klein ⓘ https://orcid.org/0000-0001-5854-675X
Patrick Dufour ⓘ https://orcid.org/0000-0003-4609-4500
Carl Melis ⓘ https://orcid.org/0000-0001-9834-7579
B. Zuckerman ⓘ https://orcid.org/0000-0001-6809-3045
Siyi Xu ⓘ https://orcid.org/0000-0002-8808-4282
Alycia J. Weinberger ⓘ https://orcid.org/0000-0001-6654-7859
Isabella L. Trierweiler ⓘ https://orcid.org/0000-0002-1299-0801
Edward D. Young ⓘ https://orcid.org/0000-0002-1299-0801

References

Adibekyan, V., Dorn, C., Sousa, S. G., et al. 2021, Sci, 374, 330
Alam, S., Albareti, F. D., Prieto, C. A., et al. 2015, ApJS, 219, 12
Andrae, R., Schulze-Hartung, T., & Melchior, P. 2010, arXiv:1012.3754
Bergeron, P., Dufour, P., Fontaine, G., et al. 2019, ApJ, 876, 67
Bianchi, L., Shiao, B., & Thilker, D. 2017, ApJS, 230, 24
Bonsor, A., Carter, P. J., Hollands, M., et al. 2020, MNRAS, 492, 2683
Buchan, A. M., Bonsor, A., Shorttle, O., et al. 2022, MNRAS, 510, 3512
Chayer, P., Fontaine, G., & Wesemael, F. 1995, ApJS, 99, 189
Coutu, S., Dufour, P., Bergeron, P., et al. 2019, ApJ, 885, 74
Cukanovaite, E., Tremblay, P. E., Bergeron, P., et al. 2021, MNRAS, 501, 5274
Debes, J. H., & Sigurdsson, S. 2002, ApJ, 572, 556
Doyle, A. E., Desch, S. J., & Young, E. D. 2021, ApJL, 907, L35
Doyle, A. E., Klein, B., Schlichting, H. E., & Young, E. D. 2020, ApJ, 901, 10
Doyle, A. E., Young, E. D., Klein, B., Zuckerman, B., & Schlichting, H. E. 2019, Sci, 366, 356
Dufour, P., Bergeron, P., Liebert, J., et al. 2007, ApJ, 663, 1291
Dufour, P., Blouin, S., Coutu, S., et al. 2017, in ASP Conf. Ser. 509, 20th European White Dwarf Workshop, ed. P.-E. Tremblay, B. Gänsicke, & T. Marsh (San Francisco, CA: ASP)
Dufour, P., Kilic, M., Fontaine, G., et al. 2010, ApJ, 719, 803
Dufour, P., Kilic, M., Fontaine, G., et al. 2012, ApJ, 749, 15
Dupuis, J., Fontaine, G., Pelletier, C., & Wesemael, F. 1992, ApJ, 82, 505
Dupuis, J., Fontaine, G., Pelletier, C., & Wesemael, F. 1993, ApJS, 84, 73
Farihi, J., Brinkworth, C. S., Gansicke, B. T., et al. 2011, ApJL, 728, L8
Farihi, J., Gänsicke, B. T., & Koester, D. 2013, Sci, 342, 218
Farihi, J., Gänsicke, B. T., Steele, P. R., et al. 2012, MNRAS, 421, 1635
Flewelling, H. A., Magnier, E. A., Chambers, K. C., et al. 2020, ApJS, 251, 7
Gaia Collaboration, Brown, A. G. A., Vallenari, A., et al. 2021, A&A, 649, A1
Gaia Collaboration, Prusti, T., de Bruijne, J. H. J., et al. 2016, A&A, 595, A1
Gale, A., Dalton, C. A., Langmuir, C. H., Su, Y., & Schilling, J.-G. 2013, GGG, 14, 489
Gänsicke, B. T., Koester, D., Farihi, J., et al. 2012, MNRAS, 424, 333
Gänsicke, B. T., Schreiber, M. R., Toloza, O., et al. 2019, Natur, 576, 61
Gentile Fusillo, N. P., Gänsicke, B. T., Farihi, J., et al. 2017, MNRAS, 468, 971
Gentile Fusillo, N. P., Tremblay, P.-E., Gansicke, B. T., et al. 2019, MNRAS, 482, 4570
Girven, J., Brinkworth, C. S., Farihi, J., et al. 2012, ApJ, 749, 154
Guidry, J. A., Vanderbosch, Z. P., Hermes, J. J., et al. 2021, ApJ, 912, 125
Harrison, J. H. D., Bonsor, A., & Madhusudhan, N. 2018, MNRAS, 479, 3814
Hollands, M. A., Gansicke, B. T., & Koester, D. 2018, MNRAS, 477, 93
Hollands, M. A., Tremblay, P. E., Gänsicke, B. T., Koester, D., & Gentile-Fusillo, N. P. 2021, NatAs, 5, 451
Hoskin, M. J., Toloza, O., Gänsicke, B. T., et al. 2020, MNRAS, 499, 171
Izquierdo, P., Gänsicke, B. T, Rodríguez-Gil, P., et al. 2023, MNRAS, 520, 2843
Izquierdo, P., Toloza, O., Gänsicke, B. T., et al. 2021, MNRAS, 501, 4276

Johnson, T. M., Klein, B. L., Koester, D., et al. 2022, ApJ, 941, 113
Jura, M. 2003, ApJL, 584, L91
Jura, M., Xu, S., Klein, B., Koester, D., & Zuckerman, B. 2012, ApJ, 750, 69
Jura, M., & Young, E. D. 2014, AREPS, 42, 45
Kelson, D. 2003, PASP, 115, 688
Kelson, D. D., Illingworth, G. D., van Dokkum, P. G., & Franx, M. 2000, ApJ, 531, 159
Klein, B., Blouin, S., Romani, D., et al. 2020, ApJ, 900, 2
Klein, B., Jura, M., Koester, D., Zuckerman, B., & Melis, C. 2010, ApJ, 709, 950
Klein, B. L., Doyle, A. E., Zuckerman, B., et al. 2021, ApJ, 914, 61
Kleinman, S. J., Kepler, S. O., Koester, D., et al. 2013, ApJS, 204, 5
Koester, D. 2009, A&A, 498, 517
Koester, D., Gänsicke, B. T., & Farihi, J. 2014, A&A, 566, 34
Koester, D., & Kepler, S. O. 2015, A&A, 583, A86
Koester, D., Rollenhagen, K., Napiwotzki, R., et al. 2005, A&A, 432, 1025
Kolecki, J. R., & Wang, J. 2022, AJ, 164, 87
Kurucz, R., & Bell, B. 1995, Atomic Line Data Kurucz CD-ROM No. 23 Cambridge, MA: Smithsonian Astrophysical Observatory
Lai, S., Dennihy, E., Xu, S., et al. 2021, ApJ, 920, 156
Limoges, M.-M., & Bergeron, P. 2010, ApJ, 714, 1037
Lodders, K. 2019, arXiv:1912.00844
McDonough, W. F. 2003, in Treatise on Geochemistry, ed. K. K. Turekian & H. D. Holland (Amsterdam: Elsevier), 547
Melis, C., & Dufour, P. 2017, ApJ, 834, 1
Melis, C., Farihi, J., Dufour, P., et al. 2011, ApJ, 732, 90
Melis, C., Zuckerman, B., Dufour, P., Song, I., & Klein, B. 2018, RNAAS, 2, 64
Putirka, K., & Xu, S. 2021, BAAS, 53, 1044
Raddi, R., Gänsicke, B. T., Koester, D., et al. 2015, MNRAS, 450, 2083
Rafikov, R. R. 2011, MNRAS, 416, L55
Redfield, S., & Linsky, J. L. 2008, ApJ, 673, 283
Rolland, B., Bergeron, P., & Fontaine, G. 2020, ApJ, 889, 87
Rudnick, R., & Gao, S. 2014, in Treatise on Geochemistry, Vol. 314 ed. H. D. Holland & K. K. Turekian (2nd edn.; Oxford: Elsevier), 1
Sheinis, A. I., Bolte, M., Epps, H. W., et al. 2002, PASP, 114, 851
Sion, E. M., Greenstein, J. L., Landstreet, J. D., et al. 1983, ApJ, 269, 253
Swan, A., Farihi, J., Koester, D., et al. 2019, MNRAS, 490, 202
Tody, D. 1986, Proc. SPIE, 627, 733
Trierweiler, I. L., Doyle, A. E., Melis, C., Walsh, K. J., & Young, E. D. 2022, ApJ, 936, 30
Unterborn, C. T., & Panero, W. R. 2019, JGRE, 124, 1704
Vanderbosch, Z., Hermes, J. J., Dennihy, E., et al. 2020, ApJ, 897, 171
Vanderbosch, Z. P., Rappaport, S., Guidry, J. A., et al. 2021, ApJ, 917, 41
Vanderburg, A., Johnson, J. A., Rappaport, S., et al. 2015, Natur, 526, 546
Van Hoof, P. A. M. 2018, Galax, 6, 63
Vennes, S., Kawka, A., & Németh, P. 2010, MNRAS, 404, L40
Vennes, S., Kawka, A., & Németh, P. 2011, MNRAS, 413, 2545
Veras, D. 2016, RSOS, 3, 150571
Vogt, S. S., Allen, S. L., Bigelow, B. C., et al. 1994, Proc. SPIE, 2198, 362
Welsh, B. Y., Lallement, R., Vergely, J.-L., & Raimond, S. 2010, A&A, 510, A54
Wesemael, F., Greenstein, J. L., Liebert, J., et al. 1993, PASP, 105, 761
Wyatt, M. C., Farihi, J., Pringle, J. E., & Bonsor, A. 2014, MNRAS, 439, 3371
Xu, S., Dufour, P., Klein, B., et al. 2019, AJ, 158, 242
Xu, S., Jura, M., Dufour, P., & Zuckerman, B. 2016, ApJL, 816, 22
Xu, S., Jura, M., Klein, B., Koester, D., & Zuckerman, B. 2013, ApJ, 766, 132
Xu, S., Zuckerman, B., Dufour, P., et al. 2017, ApJL, 836, L7
Zuckerman, B., Koester, D., Dufour, P., et al. 2011, ApJ, 739, 101
Zuckerman, B., Koester, D., Melis, C., Hansen, B. M., & Jura, M. 2007, ApJ, 671, 872
Zuckerman, B., Koester, D., Reid, I. N., & Hunsch, M. 2003, ApJ, 596, 477
Zuckerman, B., Melis, C., Klein, B., Koester, D., & Jura, M. 2010, ApJ, 722, 725